Ocean Engineering 362 (2026) 126290

Contents lists available at ScienceDirect

Ocean Engineering

journal homepage: www.elsevier.com/locate/oceaneng

Research paper

A blind comparative study on isothermal sloshing in a circular tank (CCP-WSI Blind Test Series 5)☆

S.A. Brown [a,b,*,1], S.W. Colville [a], V. Francis [a], T. Zhao [a,b,1], Y.C. Lee [a], D. Cao [o], H. Chen [j], J. Chen [a,b,1], S. Chen [h], J. Davidson [c], J. Gong [n], H. Gu [l], A. Khayyer [i], D.-H. Kim [d], W. Liu [m], M. Luo [p], R. Lyu [h], Q. Ma [e], H. Ma [h], O. Mahfoze [m], I. Pregnan Johannesen [a], Y. Qin [n], S. Shrestha [k], G. Tabor [f], R. Tan [m], E. Wahbah Makhoul [f], D. Wang [l], Y. Wang [h], H. Wei [h], S. Yan [e], K.-K. Yang [d], Y. Yang [j], H. Zeng [o], Y. Zhan [p], N. Zhang [g], D.M. Greaves [a,b,1]

[a] School of Engineering, Computing and Mathematics, University of Plymouth, Plymouth, United Kingdom
[b] Department of Engineering Science, University of Oxford, Oxford, United Kingdom
[c] Basque Center for Applied Mathematics (BCAM), Mazarredo Zumarkalea 14, Bilbao 48009, Spain
[d] Department of Autonomous Vehicle System Engineering, Chungnam National University, Daejeon, Republic of Korea
[e] School of Science & Technology, City, University of London, London, United Kingdom
[f] Faculty of Environment, Science and Economy, University of Exeter, Exeter, United Kingdom
[g] College of Shipbuilding Engineering, Harbin Engineering University, Harbin, Heilongjiang, China
[h] School of Naval Architecture and Ocean Engineering, Jiangsu University of Science and Technology, China
[i] Department of Civil and Earth Resources Engineering, Kyoto University, Kyoto, Japan
[j] School of Engineering, Newcastle University, Newcastle upon Tyne, United Kingdom
[k] Department of Civil Engineering, University of Queensland, Australia
[l] Institute of Hydraulics and Ocean Engineering (IHOE), Ningbo University, Ningbo, Zhejiang, China
[m] Daresbury Laboratory, Science and Technology Facilities Council (STFC), United Kingdom
[n] College of Ocean Science and Engineering, Shanghai Maritime University, Shanghai, China
[o] Department of Hydraulic Engineering, Tongji University, Shanghai, China
[p] Ocean College, Zhejiang University, Zhoushan, China

ARTICLE INFO

Keywords:
Sloshing
Faraday waves
Comparative study
Computational fluid dynamics
Smoothed particle hydrodynamics
Graph neural network

ABSTRACT

Numerical modelling is important in many fluid dynamics applications, yet robust benchmarking is required to quantify uncertainty. This study presents results from a blind comparative benchmark of isothermal sloshing in a circular tank. Sloshing is relevant to many engineering applications, including offshore shipping, where vessel motions can excite internal fluid motion, generating impact loads and affecting stability. A series of horizontal and vertical excitation cases of increasing complexity are considered. Participant solutions for free surface displacements are compared against physical model data that was withheld until after submission. Across all cases, the numerical models generally capture the dominant frequency. Typical errors are 10–15%, with some participants achieving 2%. For vertical excitation, larger discrepancies occur at the sidewalls, attributed to over-predicted run-up and difficulties in modelling breaking processes. Most submissions employ high-fidelity approaches with moderate spread in the results. In addition, an AI–accelerated approach was submitted, showing promising performance for less severe cases but requiring further development for extreme conditions. The results highlight that current numerical models capture the primary sloshing dynamics, but accurate representation of damping remains a challenge. These test cases provide a long-term benchmark for assessing numerical sloshing models, and are freely available through the CCP-WSI catalogue.

☆ This article is part of a Special issue entitled: 'OE_Sloshing' published in Ocean Engineering.

* Corresponding author at: Department of Engineering Science, University of Oxford, Oxford, United Kingdom.
E-mail address: scott.brown@plymouth.ac.uk (S.A. Brown).
[1] Present Address: University of Oxford (from 2/2/2026).

https://doi.org/10.1016/j.oceaneng.2026.126290
Received 4 March 2026; Received in revised form 22 May 2026; Accepted 27 May 2026
Available online 7 June 2026

1. Introduction

Numerical modelling is a vital tool for analysing wave–structure interaction problems. This has led to the development of a wide range of computational approaches, which span the full spectrum of model fidelity, with the choice of method typically driven by the trade-off between computational efficiency and the level of physical detail included. However, in many offshore applications, substantial uncertainty remains regarding the appropriate level of model fidelity required for accurately simulating interactions between waves and offshore or coastal structures.

The Collaborative Computational Project in Wave Structure Interaction (CCP-WSI) Blind Test Series aims to address this uncertainty and support the advancement of numerical modelling standards. These comparative studies invite members of the wave–structure interaction community to voluntarily apply their numerical models to a series of carefully designed test cases, representing a broad range of wave-structure interaction complexities. Each case is released as a blind test, providing sufficient detail for participants to simulate the problem. Participants submit blind numerical results, without access to the physical modelling ground truth. Submitted results are then compared with the experimental data, and the full physical modelling dataset is published, establishing a benchmark for future model development. Previous CCP-WSI comparative studies have considered wave interaction with floating production, storage, and offloading structures (Ransley et al., 2019), wave energy converters (Ransley et al., 2020a,b), and floating wind turbines (Yu et al., 2025). The present study presents the results of CCP-WSI Blind Test Series 5, which focuses on isothermal sloshing in a circular tank.

Fluid dynamic sloshing is a complex free surface phenomenon arising from the motion of liquid within partially filled tanks which are typically subjected to external excitation. Although sloshing can sometimes be quite benign, it can also produce violent responses to even small disturbances of the tank, particularly at or near resonance. Sloshing related challenges arise in a wide range of applications, including Liquefied Natural Gas (LNG) cargo tanks onboard ships and Liquid Hydrogen (LH2) fuel tanks in aircraft. In offshore shipping, vessel motions can excite the fluid contained within the tank, generating impact loads capable of damaging tank walls and modifying ship stability. Similarly, in aviation, fuel sloshing can become strongly coupled with the aircraft's global motion and influence its dynamic response. Such coupling presents significant design and operational challenges; therefore, understanding and mitigating sloshing induced loads and associated pressure variations is crucial for maintaining system stability.

Researchers have employed several approaches, including analytical, experimental and numerical methods, to investigate sloshing phenomena. However, because the focus of this paper is on the numerical modelling of sloshing, the present review is limited to studies that use computational approaches to simulate sloshing. For a broader and more comprehensive overview of sloshing theory, experiments and applications, the reader is referred to Ibrahim (2005), Faltinsen and Timokha (2009), and Ibrahim (2020).

Numerical models used to study sloshing can broadly be categorised into non-viscous and viscous formulations. Non-viscous approaches are typically based on potential flow theory and, owing to their computational efficiency, have formed the basis of several key studies in the past (Faltinsen, 1978; Faltinsen et al., 2000; Faltinsen and Timokha, 2001). However, since they neglect viscosity, these models are unable to capture several important aspects of sloshing, particularly when the fluid motion is strongly nonlinear or when there is breaking of the free surface. In contrast, viscous modelling frameworks, most notably Computational Fluid Dynamics (CFD) solutions of the Navier–Stokes Equations (NSE), are able to capture the full range of flow physics, enabling a more accurate representation of the phenomena. As computing capability has improved over recent decades, sloshing research has therefore increasingly shifted towards CFD-based numerical investigation, encompassing both mesh-based and mesh-free techniques. On the mesh-based side, the Finite Difference Method (FDM) (Chen and Nokes, 2005; Wu and Chen, 2009; Tuyen et al., 2013; Wu et al., 2013), and, more commonly, the Finite Volume Method (FVM) (Dias et al., 2007; Schreier and Paschen, 2008; Peric et al., 2009; Thiagarajan et al., 2011; Oxtoby et al., 2015; Jäger, 2019; Huang, 2023; Sanapala et al., 2024) have been used. In mesh-based NSE solvers, accurately representing the moving phase boundary requires an additional interface capturing framework. Among the most widely used approaches for this are the Volume of Fluid (VOF) method (Hirt and Nichols, 1981) and the Level Set Method (LSM) (Sussman et al., 1994). However, both of these approaches are not without its limitations. The VOF method conserves mass inherently, but because the volume fraction field behaves as a step function it can compromise the accuracy of the computed interface curvature. On the other hand, the LSM allows for smoother interface curvature calculations, but it does not conserve mass as effectively as VOF. Despite these limitations, both VOF and LSM remain widely popular and continue to be integrated into the standard FDM and, more commonly FVM, framework. In parallel, mesh-free particle methods, including the Smoothed Particle Hydrodynamics (SPH) method (Rudman et al., 2009; Colagrossi et al., 2010; Rafiee et al., 2011; Shao et al., 2012) and the Moving Particle Semi-Implicit (MPS) method (Young Yoon et al., 1999; Pan et al., 2008; Kim et al., 2014) have also been used. The reader is referred to Konar and Das (2025) for an overview of the latest developments in the numerical modelling of liquid sloshing.

This paper summarises the work submitted to the sloshing comparative study from a total of 13 contributions. The organisation of the rest of the paper is as follows: Section 2 describes the sloshing tank geometry and the experimental setup, and outlines the assessment criteria provided to the participants, including the blind test parameters; Section 3 gives a brief description of each contributing code and its underlying numerical approach(es); Section 4 discusses qualitative behaviour of the flow by comparing a representative numerical model with experimental recordings using snapshot-based comparisons; Sections 5 and 6 present quantitative assessments against the experimental measurements in the frequency and time domains, respectively, including an evaluation of numerical errors; and the conclusions from the comparative study are drawn in the final section.

2. CCP-WSI Blind Test Series 5

The present blind test is 'CCP-WSI Blind Test Series 5: Isothermal Sloshing in a Circular Tank'. A cylindrical tank, partially filled with water, is forced either horizontally or vertically, depending on the specific case. This section outlines the physical modelling setup, the sloshing behaviour observed for each case, and specifies the numerical data requested from participants.

2.1. Physical experiments

Physical modelling was conducted at the COAST Laboratory, University of Plymouth, UK, using a horizontal cylindrical tank made of transparent cast acrylic (Colville et al., 2025). The tank, with a diameter of 0.4 m and a depth of 0.04 m was partially filled with water under isothermal conditions at 20 °C and atmospheric pressure (1.013 bar), giving water and air densities of 998 kg/m^3 and 1.204 kg/m^3, respectively.

A global coordinate system (x, y, z) is defined with the origin at the tank centre (Fig. 1), where x is horizontal, y is longitudinal, and z is vertical. Sinusoidal acceleration was applied using an electromechanical actuator for both horizontal and vertical excitations. The fill level, h, is expressed as a dimensionless ratio h/D relative to the tank diameter, while the excitation amplitude, A, and driving frequency, f_d,

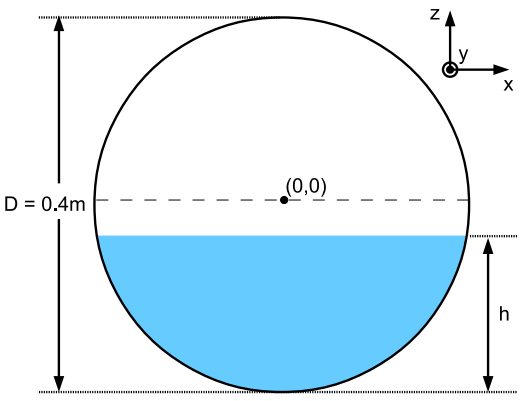

Fig. 1. Diagram of the CCP-WSI Blind Test Series 5 setup.

are given in millimetres (mm) and hertz (Hz), respectively. For horizontal excitation, the tank starts at the maximum x, with the actuator initially pushing in the negative x direction; for vertical excitation, the tank starts at the minimum z, with the actuator initially pulling in the positive z direction.

The motion of the tank and the liquid free surface were captured using a high-speed camera and subsequently analysed with an image-processing algorithm, providing measurements of the tank displacement, the global free surface shape, and the position of the fluid's centre of gravity. The maximum resolution of the camera (i.e 1 pixel) was 0.46 mm. In post-processing, the sidewall is assumed to be 5 pixels (2.3 mm) inside the wall due to increased noise at the edge of the tank.

2.2. Test cases

Six cases are reported in this work: three horizontal and three vertical excitation cases, with varying excitation frequency, amplitude and fill level. The test cases presented in Table 1 were selected from the broader experimental campaign of Colville et al. (2025), with the aim of capturing progressively increasing physical complexity, including beating, Faraday wave formation, free surface breaking, and travelling wave behaviour. The excitation frequencies were chosen close to the natural sloshing frequency (or approximately twice this value for vertically excited cases), where strongly nonlinear free surface responses are expected. The resulting case matrix was intended to provide a structured benchmark for assessing numerical approaches across a range of flow regimes and modelling fidelities, including conditions where simplified free surface treatments may begin to lose accuracy.

Participants were provided with the experimental details in Section 2.1 together with the theoretical input curves used in the experiments (CCP-WSI Working Group, 2025). This included the direction of excitation, fill level, driving frequency, amplitude and initial tank position (Table 1). The theoretical natural frequency, calculated based on the eignvalues of the geometry (McIver, 1989), and observations regarding free surface breaking are also included in Table 1 for completeness, but this information was not provided to the participants prior to submission.

2.3. Assessment criteria

Participants were asked to provide the vertical coordinate of the free surface elevation at the left and right sidewalls for all cases. For the vertical excitation cases, the free surface elevation at the tank centre ($x = 0$) was also required. In most cases, the submitted time series were requested from the start of excitation ($n_0 = 0$) and continued for a specified number of cycles N, as listed in Table 1. Cases H2 and H3 differed in that only the quasi-steady response, established after 80 cycles ($n_0 = 80$), was considered. As the blind test is conducted on a voluntary basis, not all participants submitted data for every case.

Table 1
CCP-WSI Blind Test 5 parameters: shorthand ID (ID); excitation direction (Exc.) - horizontal (H) or vertical (V); fill level (h/D); excitation amplitude (A); driving frequency (f_d); theoretical natural frequency (f_0); assessment criteria start cycle (n_0); assessment criteria number of cycles (N); and whether breaking (Br.) was observed (Y) or not (N) in the experiments. The natural frequency (f_0) and breaking observations were not provided to the participants prior to submission. All other quantities were known to participants and define the imposed experimental forcing conditions.

ID	Exc.	h/D [–]	A [mm]	f_d [Hz]	f_0 [Hz]	n_0 [–]	N [–]	Br. [–]
H1	H	0.3	2.0	1.300	1.203	0	65	N
H2	H	0.3	2.0	1.180	1.203	80	17	N
H3	H	0.7	0.5	1.450	1.471	80	21	N
V1	V	0.3	2.0	3.790	1.895	0	227	N
V2	V	0.5	4.0	3.882	1.941	0	116	Y
V3	V	0.5	8.0	3.882	1.941	0	58	Y

2.4. Physical modelling behaviour

The qualitative behaviour observed in the physical modelling was not disclosed to participants prior to the submission of their numerical predictions. This section summarises the key features of the experimental response and outlines the intended motivation for including each case in the blind test. This information can be used in conjunction with the physical modelling time series' data presented in Fig. 2 and image data presented in Figs. 3 and 4, to aid understanding.

2.4.1. H1

Case H1 is a relatively simple scenario in which the driving frequency was set slightly above the first antisymmetric frequency of the tank and the excitation amplitude kept deliberately low. This configuration produces a modest liquid free surface response while also giving rise to a characteristic beating effect (Fig. 2a) resulting from the small offset between the driving and natural frequencies.

2.4.2. H2

Case H2 investigates a more nonlinear response regime in which the physical model exhibits a pronounced asymmetry between the sidewalls (Fig. 3). This behaviour, observed consistently in the experiments, includes a travelling-wave component superimposed on the expected antisymmetric mode, although the underlying cause of the asymmetry remains unclear. This corresponds to resonance conditions, yielding the highest experimental response for the given excitation amplitude.

2.4.3. H3

Case H3 examines a higher filling level in the horizontal configuration. Although the excitation amplitude in this case is small, the liquid exhibits nonlinear behaviour, with travelling waves present despite the modest resulting wave amplitudes (Fig. 3). This response is likely associated with the concave geometry of the partially filled horizontal cylindrical tank at this fill level.

2.4.4. V1

Case V1 considers vertical excitation of the liquid, where the driving frequency is set to twice the first symmetric natural frequency of the tank. Assuming the forcing amplitude is large enough, this condition produces nonlinear free surface waves, known as Faraday waves (Benjamin and Ursell, 1954). These waves exhibit a sub-harmonic response, with the free surface oscillating at half the imposed forcing frequency (Colville et al., 2025). Under these conditions, the liquid remains quiescent for an extended initial period, exhibiting little observable sloshing (Fig. 2d). Once the instability is triggered, however, the wave amplitude grows quickly. Accurately predicting the timing of this onset poses a significant challenge for numerical models, making this case a test of their ability to capture the transition from a stable liquid state to developed liquid sloshing.

Table 2
Summary of the numerical model setups for the data provided to CCP-WSI Blind Test Series 5. ID is the naming convention used in this work. Setup Ref. is the reference to a paper associated to the blind test setup, where available. For the dimension of the numerical tank (Dim.), 3DS is a 3D tank with a symmetry condition. Free Surface treatment (Free Surf.) is either potential free surface (PFS), volume of fluid (VOF), level-set method (LSM) or auxiliary function (AF). Surface tension (Surf. Tens.) is included (yes) or neglected (no). For the time step (Δt), a condition dependent on the Courant condition (C) is adaptive, otherwise it is it fixed to the stated value. Turbulence treatment is either laminar (Lam.), RANS, LES, artificial viscosity (AV) or Riemann stabilisation (RS). The number of cells/particles used for each case is also presented ($\times 10^3$). Note the physical modelling image data includes approximately 594×10^3 pixels inside the tank.

ID	Setup Ref.	Code Name/Ref.	Dim.	Free Surf.	Surf. Tens.	Δt	Turb. Treat.	Turb. Model	# of Cells or Particles ($\times 10^3$) H1	H2	H3	V1	V2	V3
FDM1	Gu et al. (2025)	NEWTANK (Lin et al., 2016)	2D	VOF	No	$C \leq 0.1$	LES	Smagorinsky -Lilly SGS	86	86	86	86	147	–
FVM1	–	OpenFOAM (ESI OpenCFD, 2023)	3DS	PFS	No	$C \leq 0.03$	Lam.	–	11	11	82	11	57	57
FVM2	Kim and Yang (2025)	Star-CCM+ (Siemens Digital Industries Software, 2026)	3D	VOF	Yes	$C \leq 0.5$	RANS	Realizable $k-\epsilon$	80	80	80	80	80	80
FVM3a	–	OpenFOAM (ESI OpenCFD, 2023)	3D	VOF	No	$C \leq 0.5$	Lam.	–	79	79	79	79	79	79
FVM3b	–	OpenFOAM (ESI OpenCFD, 2023)	3D	VOF	Yes	$C \leq 0.5$	Lam.	–	79	79	79	79	79	79
FVM3c	–	OpenFOAM (ESI OpenCFD, 2023)	3D	VOF	No	$C \leq 0.5$	RANS	$k-\omega$ SST	79	79	79	79	79	79
FVM3d	–	OpenFOAM (ESI OpenCFD, 2023)	3D	VOF	Yes	$C \leq 0.5$	RANS	$k-\omega$ SST	79	79	79	79	79	79
FVM3e	–	OpenFOAM (ESI OpenCFD, 2023)	3D	VOF	No	$C \leq 0.5$	RANS	$k-\epsilon$	79	79	79	79	79	79
FVM3f	–	OpenFOAM (ESI OpenCFD, 2023)	3D	VOF	Yes	$C \leq 0.5$	RANS	$k-\epsilon$	79	79	79	79	79	79
FVM4a	Wang et al. (2025)	DXFlow (Wang and Dong, 2024)	2D	VOF	Yes	$C \leq 0.4$	Lam.	–	8	10	–	–	–	–
FVM4b	Wang et al. (2025)	DXFlow (Wang and Dong, 2024)	2D	VOF	Yes	$C \leq 0.2$	Lam.	–	–	–	–	72	–	–
FVM4c	Wang et al. (2025)	DXFlow (Wang and Dong, 2024)	2D	VOF	Yes	$C \leq 0.1$	Lam.	–	–	–	–	–	162	–
FVM4d	Wang et al. (2025)	DXFlow (Wang and Dong, 2024)	2D	VOF	Yes	$C \leq 0.1$	RANS	RNG $k-\epsilon$	–	–	–	–	–	128
FVM5a	Brown et al. (2026)	OpenFOAM (ESI OpenCFD, 2022)	3DS	VOF	Yes	0.2 ms	RANS	$k-\omega$ SST	500	500	500	500	500	–
FVM5b	Brown et al. (2026)	OpenFOAM (ESI OpenCFD, 2022)	3DS	VOF	Yes	0.1 ms	RANS	$k-\omega$ SST	–	–	–	–	–	5,600
FVM6	(Tan et al., 2025)	OpenFOAM (ESI OpenCFD, 2022)	3D	VOF	Yes	$C \leq 0.25$	RANS	Modified RNG $k-\epsilon$	2,000	2,000	2,000	2,000	2,000	2,000
FVM7	Qin and Gong (2025)	OpenFOAM (The OpenFOAM Foundation, 2015)	2D	VOF	No	0.1 s	RANS	$k-\omega$ SST	143	143	143	143	143	143
FVM8	Zeng et al. (2025)	OpenFOAM (ESI OpenCFD, 2018)	2D	VOF	Yes	$C \leq 0.2$	Lam.	–	50	50	50	50	50	50
GNN1	Zhang et al. (2025)	ISPH_GNN (Zhang et al., 2024)	2D	AF	No	1 ms	Lam.	–	1.3	1.3	–	–	–	–
SPH1	Chen et al. (2025)	DualSPHysics (Domínguez et al., 2022)	3D	–	No	$C \leq 0.2$	AV	$\alpha = 0.04$	468	468	–	468	614	614
SPH2	–	DualSPHysics+ (Zhan et al., 2025)	2D	–	No	$C \leq 0.2$	RS	–	25	–	–	25	25	–
SPH3	Ma et al. (2025)	DualSPHysics (Domínguez et al., 2022)	2D	LSM	No	0.2 s	AV	–	112	112	112	112	112	112

2.4.5. V2

Case V2 is similar to V1, with the driving frequency at twice the first symmetric frequency of the tank to incite Faraday waves. Compared with V1, the fill level is higher and a slightly larger wave amplitude develops, the characteristic rapid wave growth under vertical acceleration is present (Fig. 2e). Accurately capturing both the timing and the amplitude of this response remains a significant challenge for numerical models.

2.4.6. V3

Case V3 represents the most challenging vertical configuration, characterised by high-amplitude Faraday waves, rapid wave growth and the onset to wave breaking (Fig. 4). The experiments reveal higher-order modes, adding complexity to the initial liquid response. Capturing both the primary wave behaviour and the higher modes presents a stringent test of the predictive capability of numerical models.

3. Numerical models

This section summarises the numerical modelling approaches used by each of the participants. Each method is provided a unique ID (Table 2), which will be used throughout this work, and can be cross-referenced to this section. Note that due to the large number of methods, similar and relatively high-level information is provided for each, and is summarised in Table 2. As part of the blind test exercise, participants were also invited to submit accompanying papers describing their numerical approaches in greater detail. Where available, these are listed in Table 2 as 'Setup Ref.' and may be consulted by interested readers for additional information, including details of mesh design, numerical settings, and modelling choices. Readers are also referred to the corresponding 'Code Ref.' for further details regarding the underlying numerical methods and software implementations.

3.1. FDM1

NEWTANK (Liu and Lin, 2008; Lin et al., 2016), a virtual boundary force (VBF) code, was used to solve the incompressible spatially averaged Navier–Stokes (SANS) equations in a 2D domain discretised by FDM. Turbulence is represented using an LES model, and the free surface is handled using VOF. Surface tension is neglected. Two meshes were considered, depending on case: a coarser mesh consisting of 86,052 cells; a finer mesh with 147,852 cells. Simulations were run on a single core of a 13th Gen Intel i9-13900H, requiring typical runtimes of

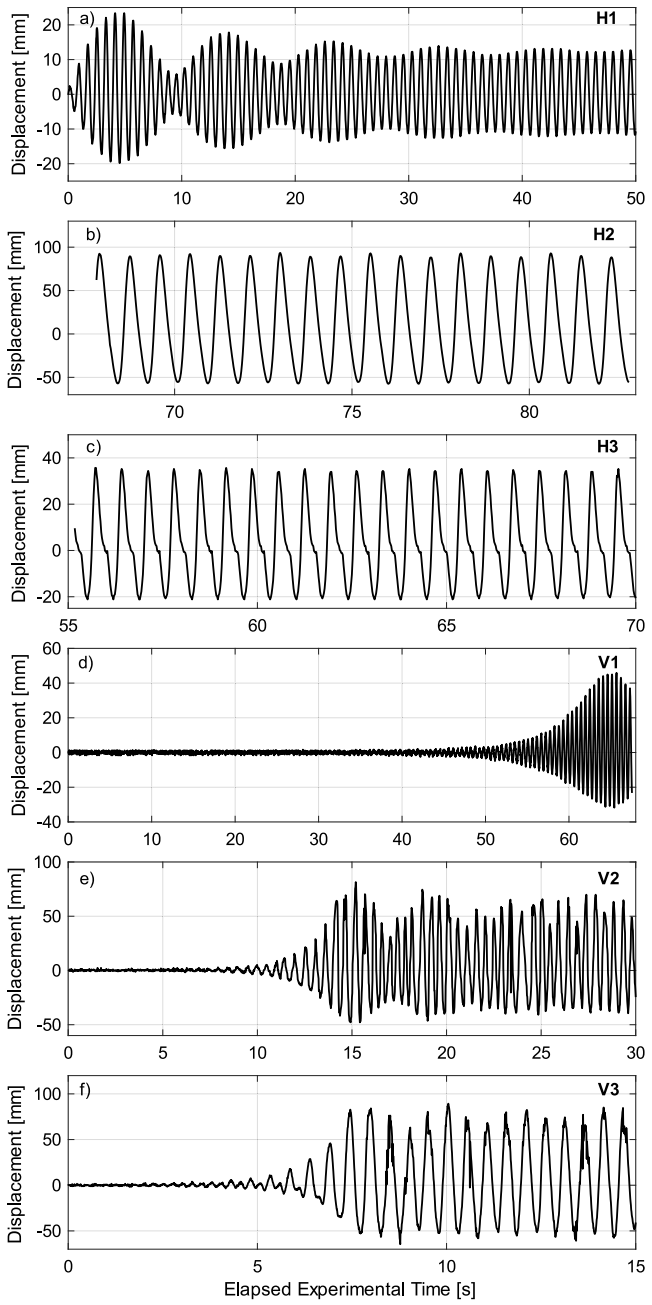

Fig. 2. Time series from physical modelling for each case. Data presented is for the right sidewall vertical displacement. Note that cases H2 and H3 focus on the quasi-steady state and hence do not start at the temporal origin of the experiments.

10-20 h on the coarser mesh, and 48 h on the finer mesh. Time stepping is adaptive and is based on a maximum Courant number of 0.1.

3.2. FVM1

OpenFOAM-v2312 (Weller et al., 1998; ESI OpenCFD, 2023) solution using the potentialFreeSurfaceFoam application to solve the incompressible RANS equations in a 3D symmetry domain discretised by FVM. Simulations were run in laminar mode. Surface tension is neglected. The free surface boundary uses a condition that calculates the change in surface elevation at each time step based on the volume flux in the cells at the free surface boundary. The pressure field is then modified due to the change in free surface elevation via the hydrostatic pressure equation. Depending on the case, the model employs 11,000–82,000 cells, with simulations run on a desktop requiring a runtime of 1-5 hours on a single core. Time stepping is adaptive based on a maximum Courant number of 0.031.

3.3. FVM2

Simcenter STAR-CCM+ 23.06 (Siemens Digital Industries Software, 2026) solution for the incompressible RANS equations in a 3D domain discretised by FVM. Turbulence is represented using the Realizable $k-\epsilon$ turbulence model and the free surface is handled via the VOF method. Surface tension is included. The simulations consisted of 80,000 cells, with simulations run on an in-house HPC service requiring 10 hours on 16 cores. Time stepping is adaptive based on a maximum Courant number of 0.5.

3.4. FVM3

OpenFOAM-v2312 (Weller et al., 1998; ESI OpenCFD, 2023) solution using the interFoam application to solve the RANS equations in a 3D domain discretised by FVM. Six model variants were supplied: a laminar configuration without surface tension (FVM3a) and with surface tension (FVM3b); $k-\omega$ SST turbulence model without (FVM3c) and with (FVM3d) surface tension; and $k-\epsilon$ turbulence model without (FVM3e) and with (FVM3f) surface tension. Surface tension is modelled via the Continuum Surface Force model (Brackbill et al., 1992). The free surface is modelled using the VOF method. All variants use 78,600 cells (resolution of 4 mm), with simulations run on a workstation (CPU: Intel Core i9-14900K, RAM of 125 GB) and requiring approximately 1-2 hours. Adjustable time stepping is utilised based on a maximum Courant number of 0.5.

3.5. FVM4

DXFlow (Wang and Dong, 2024), which is an open-source code developed at Ningbo University based on the OpenFOAM-v2006 (Weller et al., 1998; ESI OpenCFD, 2020) solution, was used with the DXIsoFlow application to solve the incompressible RANS equations in a 2D domain discretised by FVM. Except for the V3 case, where the RNG $k-\epsilon$ model was used (FVM4d), all simulations were run in laminar mode (FVM4a-c). Surface tension is included, and the free surface is captured using the VOF method. The mesh size varies between cases, ranging from 8,000 to 162,000 cells, with details provided in Table 2. Simulations were run on a workstation (CPU: AMD Epyc 7763, RAM of 512 GB) with typical runtimes of 1-10 hours on 4 cores, depending on the intensity of the sloshing. Time stepping is adaptive and is based on a maximum Courant number, which was 0.4 for H1–H2 (FVM4a), 0.2 for V1 (FVM4b), and 0.1 for V2–V3 (FVM4c).

3.6. FVM5

OpenFOAM-v2212 (Weller et al., 1998; ESI OpenCFD, 2022) solution using the interFoam application to solve the RANS equations in a 3D symmetry domain discretised by FVM. Turbulence is represented using the $k-\omega$ SST turbulence closure model and the free surface is handled via the VOF method. Surface tension is included. Two model variants were provided: the coarser mesh case (FVM5a) with 500,000 mesh cells and the finer mesh case (FVM5b) with 5,600,000 mesh cells. Simulations were run on Archer2, the UK national supercomputing service, with typical runtimes of 10-18 h (FVM5a) and 27 h (FVM5b). Time stepping is fixed with a step size of 0.2 ms and 0.1 ms for FVM5a and FVM5b, respectively.

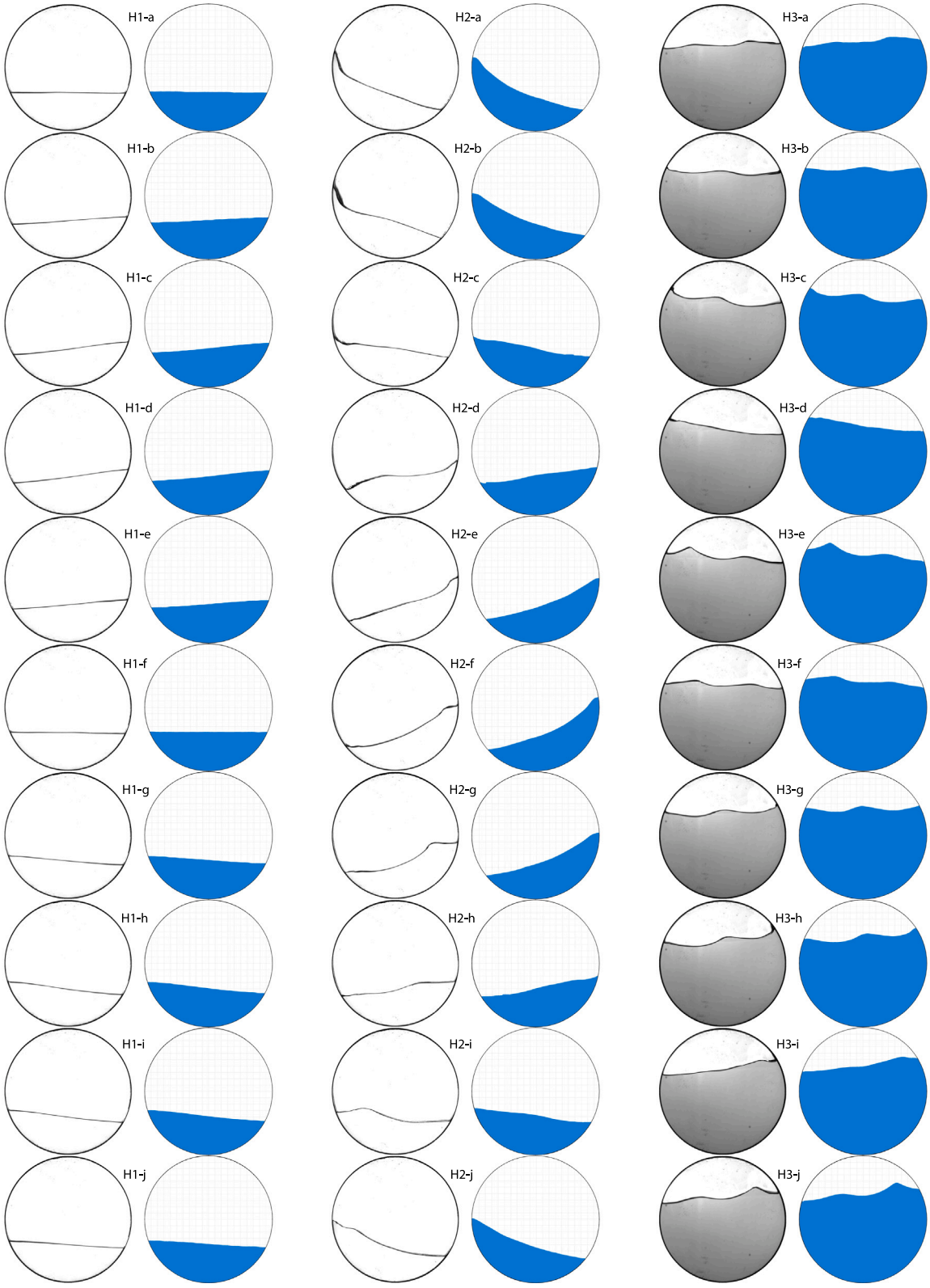

Fig. 3. Qualitative comparison of the physical and numerical response cycle for the global free surface for each horizontal excitation case (left to right: H1, H2, and H3). For each comparison, the physical result is on the left and the numerical response, achieved using FVM5, is on the right. Both the physical and numerical results show a single representative response cycle. The cycle indices may differ, however, due to differences in excitation onset.

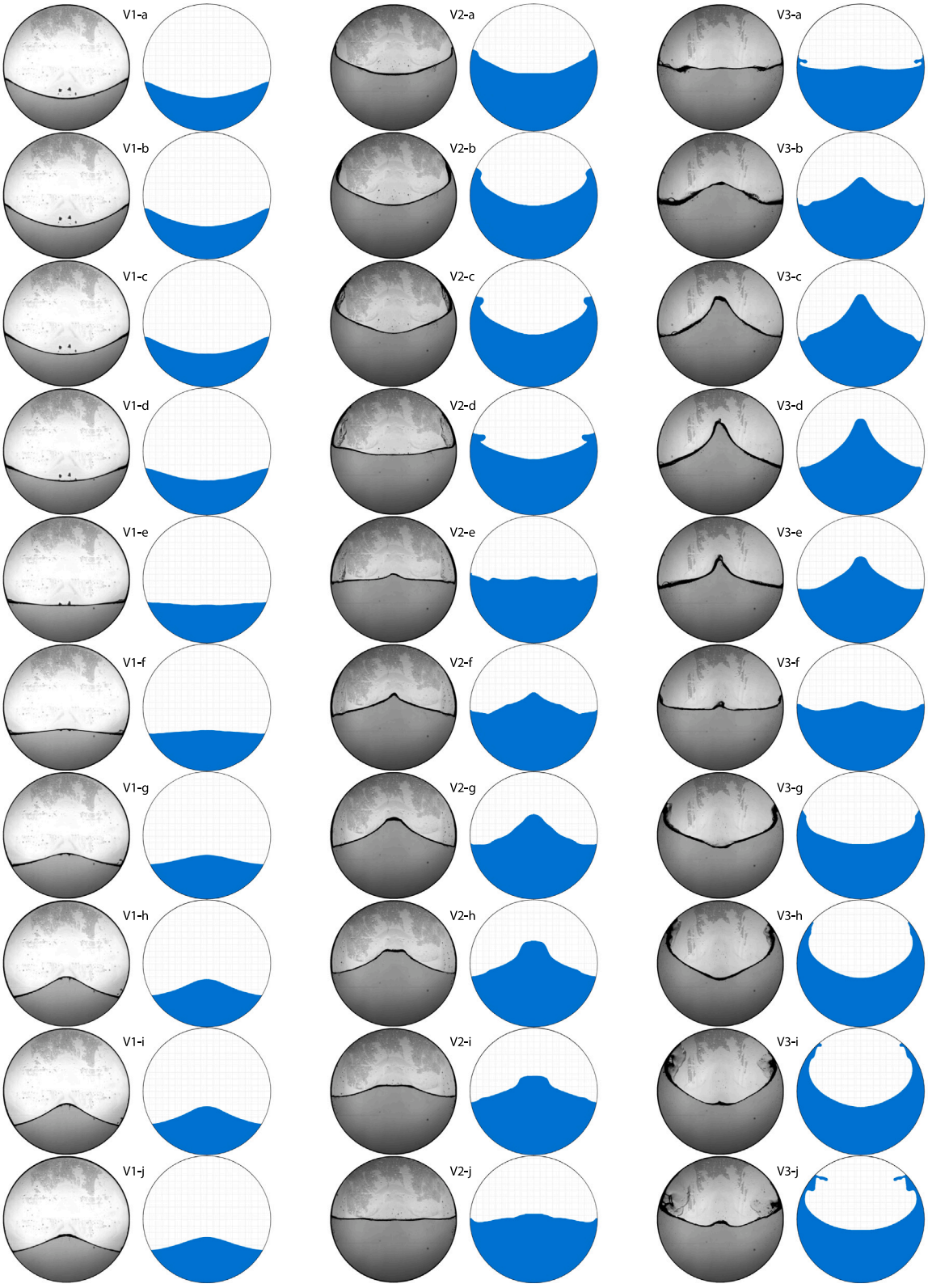

Fig. 4. Qualitative comparison of the physical and numerical response cycle for the global free surface for each vertical excitation case (left to right: V1, V2, and V3). For each comparison, the physical result is on the left and the numerical response, achieved using FVM5, is on the right. Both the physical and numerical results show a single representative response cycle. The cycle indices may differ, however, due to differences in excitation onset.

3.7. FVM6

OpenFOAM-v2212 (Weller et al., 1998; ESI OpenCFD, 2022) solution using the interFoam application to solve the RANS equations in a 3D domain discretised by FVM. Turbulence is represented using Modified RNG $k-\epsilon$ turbulence closure model and the free surface is captured via the VOF method. Surface tension is included. The model employs 2,040,000 cells, and the simulations were run on Archer2, the UK national supercomputing service, using 2 nodes (2 x 128 cores) with runtimes ranging from 100 h (H1) to 150 h (V3). Time stepping is adjustable with a maximum Courant number of 0.25.

3.8. FVM7

OpenFOAM-v3.0.0 (Weller et al., 1998; The OpenFOAM Foundation, 2015) solution using the interFoam application to solve the incompressible RANS equations in a 2D domain discretised by FVM. Turbulence is represented using the $k-\omega$ SST turbulence closure model and the free surface is captured via the VOF method. Surface tension is neglected. The model employs 143,000 cells, and the simulations were run on a GPU accelerated workstation using 8 cores with runtimes ranging from 10 h ($V3$) to 36 h ($H3$). Time stepping is fixed with a step size of 0.1 s.

3.9. FVM8

OpenFOAM-v1812 (Weller et al., 1998; ESI OpenCFD, 2018) solution using the interFoam application to solve the incompressible RANS equations in a 2D domain discretised by FVM. Simulations were run in laminar mode and surface tension was included. The model employs 50,000 cells, and the simulations were run on a workstation using 16 cores, with runtimes ranging from 3 to 5 h. Time stepping is adaptive with a maximum Courant number of 0.2.

3.10. GNN1

ISPH_GNN (Zhang et al., 2024) was used to obtain a single phase 2D solution using the incompressible SPH (ISPH) formulation, in which the Lagrangian form of the NSE are discretised on a mesh-free domain. In ISPH_GNN, the trained graph neural network (GNN) model is used to replace solving the pressure Poisson's equation (PPE), which is the most time-consuming, in the conventional ISPH. The GNN model was trained using data generated from dam breaking and sloshing in rectangle tank case. The air phase was not modelled, and turbulence was not explicitly simulated. The free surface is handled via auxiliary functions (AF) related to the particle distribution and the particle density. Surface tension was neglected. An initial particle spacing of 0.005 m and a fixed time step of 0.001 s were employed. The model employs about 1300 particles, and simulations were run on a GPU (NVIDIA GeForce RTX 3090) enhanced workstation, with typical runtimes of 0.35 h for the H1–H2 cases.

3.11. SPH1

DualSPHysics v5.2.2 (Domínguez et al., 2022) was used to obtain a single phase 3D solution using the weakly compressible SPH (WCSPH) formulation, in which the Lagrangian form of the NSE are discretised on a mesh-free domain. The air phase was not modelled. Artificial viscosity (AV) is used to stabilise the model, with a coefficient (α) value of 0.04. Surface tension is neglected. An initial particle spacing (dp) of 0.002 m was used, with a speed of sound coefficient of 20. Variable time stepping was used, controlled via a maximum Courant number condition of 0.2. The model employs 150,000 to 443,000 fluid particles and 318,000 boundary particles, and simulations were run on a desktop workstation equipped with NVIDIA RTX A2000 GPUs (12 GB), with typical runtimes of 16-60 h for the H cases and 15-42 h for the V cases.

3.12. SPH2

DualSPHysics+ (Zhan et al., 2025), an enhanced version of DualSPHysics (Domínguez et al., 2022), was used to obtain a single-phase 2D solution using the WCSPH formulation, in which the Lagrangian form of the NSE are discretised on a mesh-free domain. The air phase was not modelled. Turbulence was not modelled explicitly; instead, numerical stabilisation of the momentum equation was achieved through a Riemann stabilisation (RS) term. Surface tension was neglected. An initial particle spacing (dp) of 0.005 m was used, with a speed of sound coefficient of 10. Time stepping is variable and is controlled by a maximum Courant number of 0.2. The model employs 25,000 particles, and simulations were run on a GPU enhanced workstation using 16,384 CUDA cores, with typical runtimes of 0.81 h.

3.13. SPH3

DualSPHysics v5.2.2 (Domínguez et al., 2022) was used to obtain a multiphase 2D solution using the WCSPH formulation, in which the Lagrangian form of the NSE are discretised on a mesh-free domain. Both water and air are modelled as weakly compressible phases, and the air–water interface is captured using the LSM. Surface tension was included and turbulence was not modelled explicitly. An initial particle spacing (dp) of 0.001 m was used, with a speed of sound coefficient of 10. A fixed time step of 0.2 s was used. The model employs 112,000 particles, and simulations were run on a GPU (NVIDIA GeFORCE RTX 4060Ti) enhanced desktop workstation using 4,352 CUDA cores, with typical runtimes of 10 h.

4. Qualitative behaviour

Although CCP-WSI Blind Test Series 5 is designed around point-based quantitative metrics, additional qualitative information can be valuable for interpreting model performance. In particular, point measurements alone may not fully reflect how well a model reproduces the global free surface evolution, especially in highly transient or spatially complex flow regimes. To provide further context for the quantitative results, video snapshots of the experimental free surface (Figs. 3 and 4) are therefore included and compared with numerical predictions. This comparison is restricted to FVM5, for which full-field free surface data were available, and should be considered a representative example. While this free surface data was not requested as part of the blind test, it is presented here to provide an indication as to the extent that the overall free surface shape and dynamics are captured by the model.

Considering the horizontal cases (Fig. 3), the free surface is generally captured well. Prior to the blind test, H3 was anticipated to be the most challenging horizontal excitation case to simulate due to the observed nonlinearities in the physical modelling. However, FVM5 captures the qualitative behaviour of the free surface displacements, exhibiting the travelling wave and nonlinearities throughout the full response cycle. Case H2 on the other hand does exhibit discrepancies with respect to the physical result. In the experimental free surface snapshots, a localised near-wall interface perturbation is visible adjacent to the left sidewall early in the cycle (Fig. 3: H2-a), and a comparable, somewhat less pronounced offset emerges at the right sidewall later in the cycle (Fig. 3: H2-f). This is consistent with a free surface that advances and recedes asymmetrically on the two walls. By contrast, no analogous feature is present at either sidewall at any stage of the corresponding numerical sequence, wherein the interface meets the wall as a single, smoothly varying curve that is near-symmetrical. Furthermore, the travelling wave is much less pronounced in the numerical solution (Fig. 3: H2-d and H2-i). For the vertical excitation cases (Fig. 4), the numerical predictions of the free surface have similarities in shape to the physical modelling. As the excitation increases in complexity, there is progressively increased differences in magnitude of the response, particularly at the sidewalls (Fig. 4: V1-c,

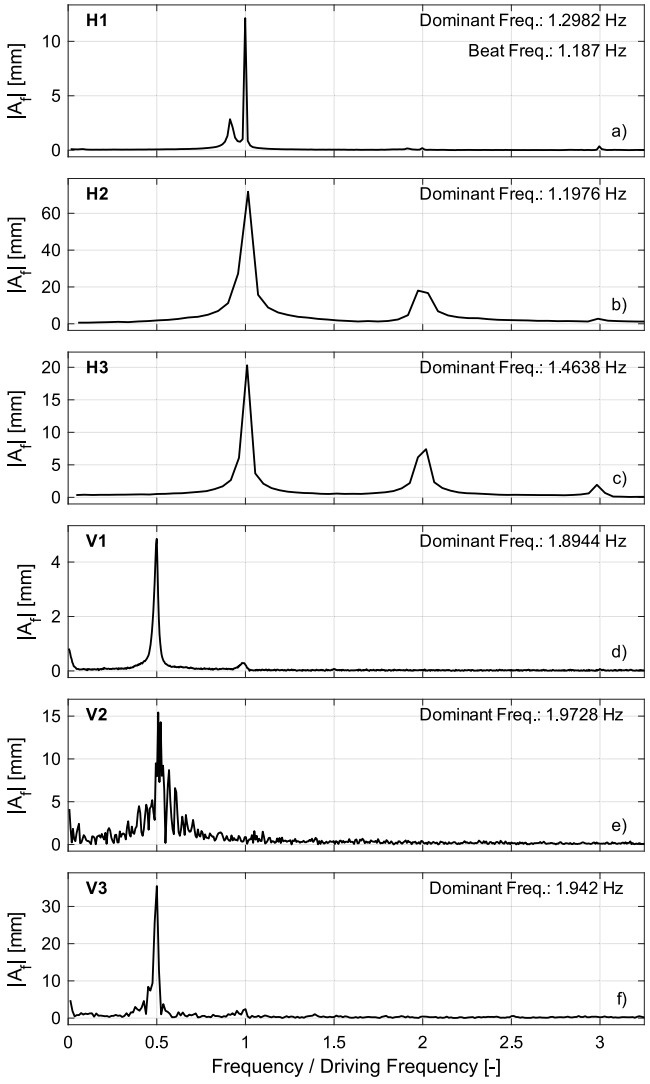

Fig. 5. FFTs for the physical free surface displacement data collected at the right sidewall. The frequency axis is normalised by the driving frequency. Each subplot represents a different case: H1 (a), H2 (b), H3 (c), V1 (d), V2 (e), and V3 (f). The stated dominant frequency is calculated as the frequency with largest magnitude.

V2-b and V3-h) and centre (Fig. 4: V1-i, V2-g and V3-d). For the most extreme case the breaking processes are not captured accurately (Fig. 4: V3-i and V3-j), and there are clear discrepancies in the magnitude of the run-up (Fig. 4: V3-h), the separation of the fluid (Fig. 4: V3-j), although the bulk of the fluid is reasonably well captured. Given the complexity of the free surface in this case, however, the discrepancy in the frame rate (V3: numerical 100 fps; physical 125 fps) could partially account for some of these discrepancies. Overall, FVM5 compares well qualitatively with the physical image data, implying that the sloshing dynamics are captured accurately by the model. Note that this is simply a representative example that can be used as context for the quantitative analysis to follow.

5. Frequency-domain analysis

Fig. 5 presents spectra of the physical data for each case, obtained via an FFT approach. The horizontal cases (Figs. 5a–c) exhibit a dominant frequency near the driving frequency, along with higher order harmonics. Case H1 (Fig. 5a), exhibits the beating phenomenon

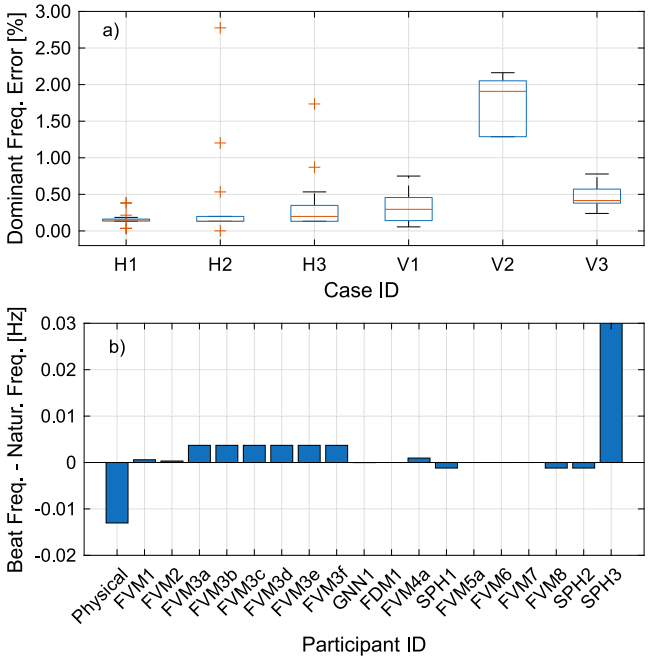

Fig. 6. Box plots showing the distribution of the errors in dominant frequency prediction for each test case across the numerical solutions (a). The central (red) line in each box denotes the median error, the boxes indicate the interquartile range, the whiskers denote the data range excluding outliers, and outliers are shown using "+" symbols. Difference between the beat and natural frequency in case H1 for physical and numerical solutions (b).

arising from the proximity of the driving and natural frequencies. The dominant spectral peak occurs at the driving frequency near 1.3 Hz, accompanied by small harmonics at two and three times this value. A further peak at approximately 1.187 Hz lies close to the first anti-symmetric frequency of the tank (1.2 Hz), indicating clear interaction between the system's forced and natural modes. For the vertical cases (Figs. 5d–f), the dominant fluid response occurs at exactly half the driving frequency. This confirms the presence of Faraday waves, in which the free surface oscillates at half the excitation frequency when the system is driven at twice its natural frequency.

Considering the numerical results, Fig. 6a presents box plots showing the distribution of the errors in dominant frequency prediction for each test case across the numerical solutions, relative to the physical data. The median error, indicated by the central (red) line in each box, for the numerical model dominant frequencies is typically within 0.5% of the driving frequency, producing a tight distribution with minimal error. An exception is the case V2, which has a median error of 1.9% likely linked with the additional noise in the spectra for this case (Fig. 5e), and larger spread in the results. The vertical cases generally exhibit slightly larger errors than the horizontal cases, but the majority of submissions reproduce the half-frequency response characteristic of Faraday waves.

Fig. 6b presents the difference in beat and natural frequency in case H1 for each model. Most numerical models capture the natural frequency of the tank effectively. Interestingly, the physical measurement of the beat frequency contains slightly larger error than many numerical predictions, likely due to the lower temporal resolution of the physical imaging (50 fps) compared with numerical outputs, which commonly use around 100 fps. Nonetheless, the ability of the models to identify the natural frequency despite it not being specified as an input condition stands out as a noteworthy result.

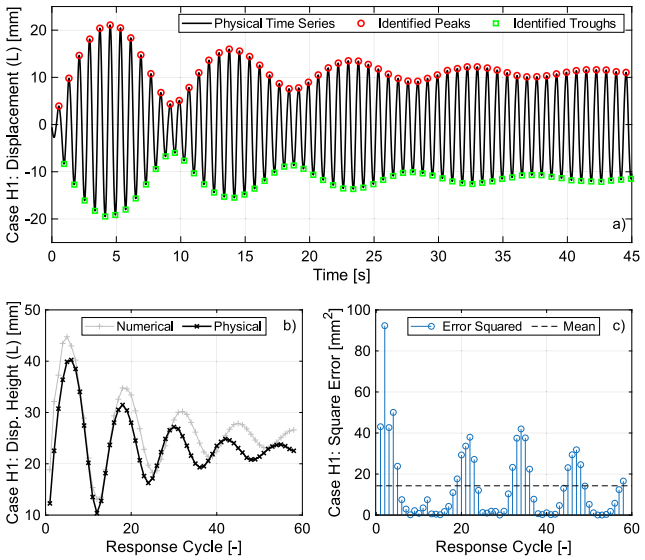

Fig. 7. Representative example of the NRMSE calculation using the left sidewall displacement data (L) for case H1. The peaks and troughs are identified (a) and used to define a displacement height (b), $\mathcal{H}$, for both the physical (black) and numerical (grey) solution. The RMSE is then calculated using the squared difference between the physical and numerical solution for $\mathcal{H}$ (c), and normalised by maximum $\mathcal{H}$ for the physical solution.

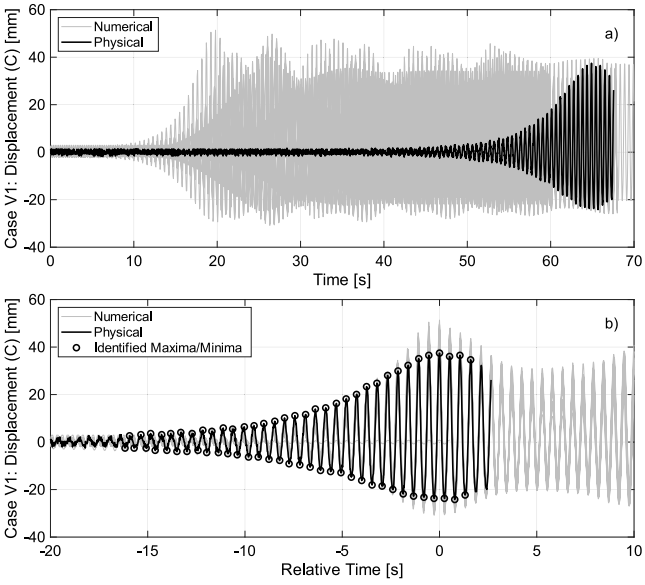

Fig. 8. Representative example of the alignment process used in the vertical excitation cases prior to the NRMSE calculation. Due to large differences in the onset of excitation between the physical (black) and numerical (grey) solutions (a), the data has been aligned such that the maximum displacement in the first group is aligned (b). This example uses displacement data for the tank centre (C) from case V1.

6. Time-domain analysis

6.1. NRMSE definition

The Normalised Root Mean Square Error (NRMSE) is used to quantify agreement between participant data and physical measurements. For horizontal excitation, the amplitude envelope of each signal is extracted by identifying successive maxima and minima between zero up-crossings (Fig. 7a). A displacement height, $\mathcal{H}$, is defined as the difference between each maximum and minimum. The NRMSE is calculated on $\mathcal{H}$ (Figs. 7b and 7c), allowing minor phase variations between individual peaks to be tolerated while capturing overall differences in the envelope. The maximum $\mathcal{H}$ observed in the experiment is used as the normalisation value in each case.

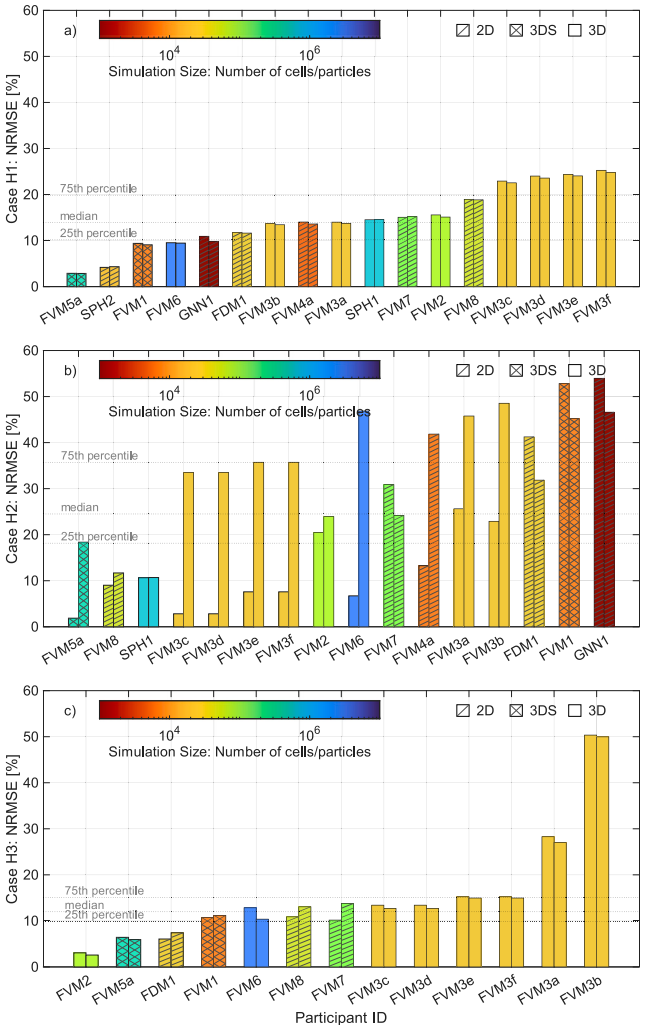

Fig. 9. NRMSE for the horizontal excitation cases: H1 (a), H2 (b) and H3 (c). Each group of bars is for a single participant's solution and represents the error at the left sidewall (left bar), and right sidewall (right bar). The bars are coloured by number of cells or particles, depending on method used, with single hatching representing 2D simulations, double hatching 3D simulations with a symmetry plane, and no hatching representing 3D simulations. The dotted lines represent the quartiles of the distribution of numerical results, which was calculated for an average of the two assessment criteria (left, right) provided by each participant.

6.1.1. Vertical excitation alignment

For vertical excitation, the onset of excitation can differ substantially between models and experiments (Fig. 8a; Section 6.3.1). The analysis therefore considers the shape of the response once excitation is observed. This is achieved by aligning the maximum of the first group of peaks (Fig. 8b) and selecting a set number of cycles before and after this point, with the number of cycles adjusted according to the duration of each case. The NRMSE is then calculated on the resulting $\mathcal{H}$ variable.

Table 3
Median, mean, inter-quartile range (IQR) and standard deviation (Std) for the NRMSE distribution across the numerical solutions. The individual assessment metrics (left, right, centre) are presented along with the average discrepancy across the metrics. All values are percentages.

		H1	H2	H3	V1	V2	V3
Left	Median	14.03	11.96	12.84	13.62	14.06	30.37
	IQR	9.36	21.10	6.01	6.63	8.83	15.79
	Mean	14.77	19.39	15.08	15.40	15.69	30.34
	Std	6.65	17.31	12.22	10.41	8.05	8.95
Right	Median	13.75	34.61	12.72	13.60	14.36	29.15
	IQR	10.04	21.44	5.33	6.77	10.63	8.91
	Mean	14.51	33.38	15.13	15.69	16.00	29.89
	Std	6.57	12.51	11.95	10.30	7.60	7.13
Centre	Median	–	–	–	9.47	10.00	11.82
	IQR	–	–	–	4.90	6.57	7.28
	Mean	–	–	–	11.50	11.35	14.41
	Std	–	–	–	10.21	6.30	4.89
Average	Median	13.87	24.50	11.97	12.25	12.06	24.49
	IQR	9.70	17.55	5.20	5.24	6.87	7.94
	Mean	14.64	26.38	15.11	14.20	14.35	24.88
	Std	6.61	12.46	12.06	10.07	6.61	5.04

6.2. Horizontal excitation results

Fig. 9 presents the NRMSE for the horizontal excitation cases: H1 (a), H2 (b) and H3 (c). Each group of bars is for a single participant's solution and represents the error at the left sidewall (left bar), and right sidewall (right bar). The dotted lines represent the quartiles of the distribution of numerical results, which was calculated for an average of the two assessment criteria (left, right) provided by each participant ('Average' in Table 3). Table 3 presents per case statistics for the distribution of the error: median, inter-quartile range (IQR), mean, and standard deviation.

Considering case H1 (Fig. 9a), most numerical models provide a good representation of the sloshing envelope, with the left and right sidewall elevations showing broadly consistent behaviour across simulations (Table 3). The mean/median of all the numerical solutions is approximately 14%, with relatively small spread (IQR 10%; standard deviation 6%) indicating that this case is relatively insensitive to numerical model choice and setup. There are, however, two solutions (FVM5a, SPH2) that achieve slightly better agreement (< 5%). There are no clear setup differences for these two, and is likely to be linked to capturing the damping more accurately than other models (see Section 6.2.1).

For case H2 (Fig. 9b), the results for the left sidewall are captured well by many of the numerical models, with a median result of 12%. There is considerably more variation (IQR 21%; standard deviation 17.31%) than observed in case H1 (Table 3), indicating choice of model and setup are more influential in this case. For the right sidewall, most of the numerical models do not reproduce the asymmetry observed in the physical modelling (see Section 2.4), and this influences the NRMSE considerably; The median NRMSE for the right sidewall is 34%, three times that observed for the left sidewall. Analysis of right-to-left sidewall amplitude ratios demonstrates that only three solutions (FVM2, FVM7 and FVM8) exhibit the same qualitative behaviour observed in the experiments (larger displacements at left sidewall), and these exhibit a smaller offset in amplitudes. The remaining models either predict near equal displacements at both sidewalls (5 solutions), or the opposite trend (smaller displacements at left wall; 7 solutions). The discrepancy between the qualitative behaviour of the numerical models needs investigating in future work, along with further analysis of the physical result, as does the influence of user-defined parameters.

Case H3 involves a relatively full tank in which a travelling wave forms along the free surface. Although this configuration is expected to be the most challenging of the horizontal cases, most numerical approaches perform well. Errors across submissions generally remain below 15% (median is 12%; Table 3), with relatively small spread (IQR 5%–6%) and little notable difference between the left and right sidewall displacements. Two clear outliers appear, both associated with laminar 3D simulations carried out on comparatively coarse meshes, suggesting that mesh resolution and turbulence modelling choices are likely contributors to the reduced accuracy in these instances.

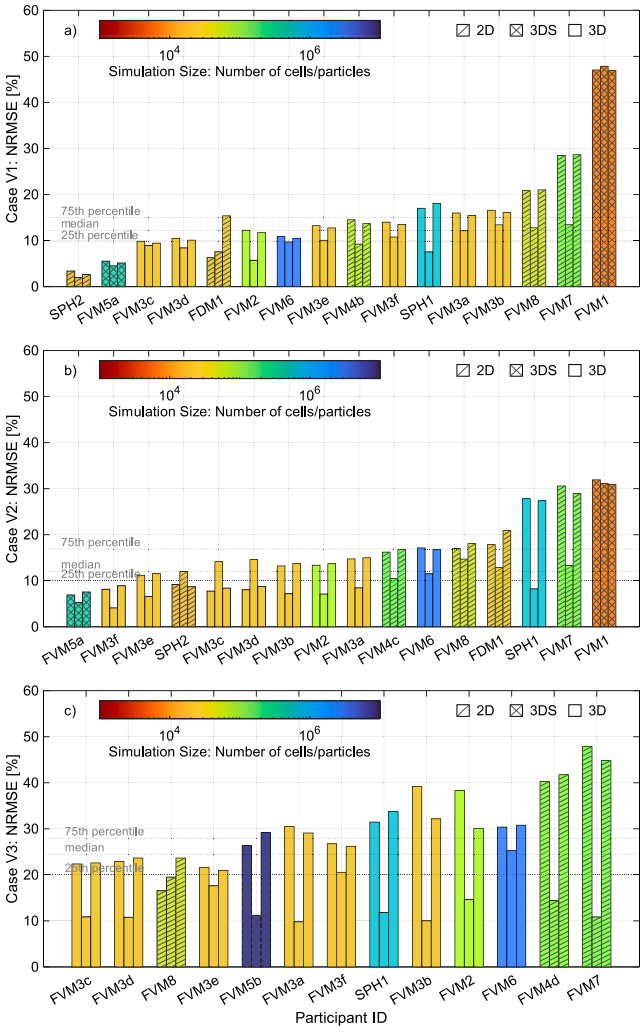

Fig. 10. NRMSE for the vertical excitation cases: V1 (a), V2 (b) and V3 (c). Each group of bars is for a single participant's solution and represents the error at the left sidewall (left bar), centre (centre bar), and right sidewall (right bar). The bars are coloured by number of cells or particles, depending on method used, with single hatching representing 2D simulations, double hatching 3D simulations with a symmetry plane, and no hatching representing 3D simulations. The dotted lines represent the quartiles of the distribution of numerical results, which was calculated for the average of the three assessment criteria (left, right, centre) provided by each participant.

6.2.1. Beat frequency damping

The beat frequency has been shown to be captured well (Section 5) but this section considers the damping of the beating. Examination of the time series for the numerical solutions indicates that not all models reproduce the damping of the beating response observed in the physical measurements. To investigate this, the largest peak in each of the first four groups in the beat envelope were extracted from each submission, enabling direct comparison of damping behaviour throughout the simulation. While some models exhibit a more linear decay in peak

amplitude, others replicate the experimentally observed quadratic-type reduction. A quadratic fit to the experimental data supports the latter trend.

One working hypothesis is that differences in dimensionality (2D versus 3D simulations) and mesh resolution influence the ability to capture damping, particularly where coarse near-wall cell sizes limit the representation of wall-related dissipation. This will be considered further in future work.

6.2.2. Alternative approaches

Although all models are included in the overall assessment, the majority adopt closely related, widely established approaches (FVM/FDM with VOF or SPH). Therefore, this section focuses on the two models that explore alternative formulations whose relative performance motivates an interesting discussion.

The FVM1 solution, obtained using a Navier–Stokes approach with a simplified potential flow based free surface boundary condition, has strong agreement with the physical data for the H1 and H3 cases. The error is around the 25th percentile for both cases, outperforming many of the FVM-VOF solutions. However, it does not capture the dynamics of H2 accurately, exhibiting an error of 49%. Of all cases considered, H1 is the most naturally suited to the simplified free surface treatment employed in FVM1, owing to its relatively small displacement amplitudes. In contrast, the performance for H3 is more unexpected, given the increased complexity of the free surface dynamics, including a travelling wave and significant nonlinear effects (Figs. 3 and 5). The error in case H2 is attributed to a significant under-prediction. FVM1 is single phase, with the free surface boundary fixed and an analytical boundary condition applied. Therefore, the model does not take into account wetting/drying of cells around the free surface. Given the large run-up exhibited in H2, this likely contributes to the reduced accuracy observed for this case. A working hypothesis is that the lower fill level compounds the issue due to the larger wall curvature.

The GNN1 solution, utilises a graph neural network approach trained using incompressible SPH. Artificial intelligence offers an exciting opportunity to accelerate high-fidelity numerical modelling, which could potentially be hugely beneficial to many fluid dynamic applications. The code used to produce GNN1 has been successfully demonstrated for applications such as solitary waves and dam breaks (Zhang et al., 2024), and has also been applied to a related sloshing problem in a rectangular tank. The present blind test therefore provides an opportunity to assess the approach in a setting where model parameters are fixed a priori. The model results are promising for case H1, capturing the amplitude well, leading to an error of 10%. However, when the time series is considered it is observed that the first beat is captured well but then settles rapidly towards a steady state, indicating excessive damping relative to the experiment. For case H2, the model has a much larger discrepancy, which could be due to lack of training data for the large amplitudes observed in this case.

6.2.3. User setup sensitivity

With six variations of the FVM3 solution available, their relative performance can be assessed under an identical, unchanged setup. The variations use different turbulence treatment: laminar (a,b); $k-\epsilon$ (c,d); and $k-\omega$ (e,f). For each turbulence model the effect of surface tension is considered (a,c,e: neglected; b,d,f: included). In H1, the laminar solution (error 15%) outperforms the RANS solutions (error 25%), potentially due to excessive damping introduced by the turbulence model. On the other hand, for H2 and H3 the RANS solutions are significantly better (more than 10% less error) than the laminar. This indicates turbulence is necessary for these cases. The model results for cases considered here are relatively insensitive to the inclusion of surface tension, with the exception of the laminar variant (FVM3a,FVM3b) in case H3.

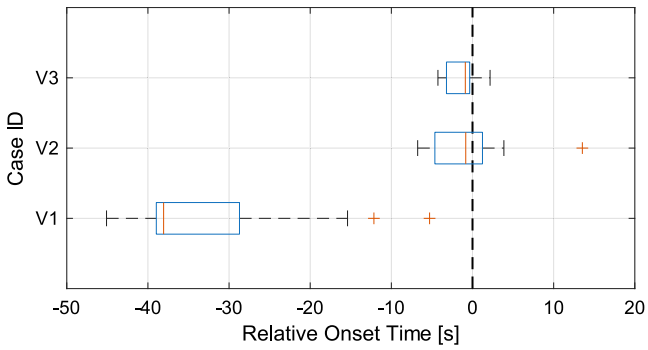

Fig. 11. Box plots showing the distribution of errors in relative onset time for each of the vertical excitation test cases across the numerical solutions. This is calculated using the maximum of the first group of peaks, and is relative to the physical result. The data shown is for the centre of the tank.

6.3. Vertical excitation results

Fig. 10 presents the NRMSE for the vertical excitation cases: V1 (a), V2 (b) and V3 (c). Each group of bars is for a single participant's solution and represents the error at the left sidewall (left bar), centre (centre bar), and right sidewall (right bar). The dotted lines represent the quartiles of the distribution of numerical results, which were calculated for an average of the three assessment criteria (left, centre, and right) provided by each participant ('Average' in Table 3).

Across cases V1 and V2, most numerical approaches reproduce the wave shape and amplitudes with good consistency, with a median error of 12% (Table 3), and relatively small variation between the models (IQR 5%–6%). An exception, however, is the potential free surface model (FVM1), which uses a single-phase RANS formulation with free surface tracking via an explicit elevation field, which performs less well than the full VOF approaches, particularly for V1. However, it is noted that for V2 it aligns more closely with the upper range of their results, which is an outcome that is somewhat unexpected given the presence of localised breaking and increased run-up at the sidewall. Given the increased fill level in V2 (Table 1), this may provide further evidence that the model struggles to capture the run-up in cases with large curvature (see Section 6.2.2).

As expected prior to the study, case V3 exhibits the highest errors of all of the cases considered within the blind test. This can largely be attributed to increased discrepancies at the left and right sidewalls, where there is significant run-up and breaking (Fig. 4), rather than at the centre of the tank. The centreline response remains comparatively well captured, but the sidewall elevations show substantial overestimation across the numerical submissions. This pattern reflects the increased complexity of the flow in this strongly breaking regime, where detached fluid fragments, spray, and intermittent overturning make the wall response highly sensitive to how the interface is interpreted. A key contributor to the increased sidewall errors is the inherent difficulty in defining the free surface within breaking regions where the fluid separates from the main bulk. Since no uniform method for identifying the free surface was specified in the blind test, differing interpretations of the interface during breaking likely amplified the scatter observed in the results.

6.3.1. Onset of excitation

As previously discussed, for the vertical excitation cases the onset of significant motion occurs only after a prolonged quiescent period (e.g. Fig. 8). Fig. 11 presents the distribution of the time of the maximum of the first group of peaks, which was used for alignment of the vertical excitation time series (Section 6.1.1). For cases V2 and V3 the numerical models typically exhibit reasonable agreement with the physical model (median $\approx -0.8\,\mathrm{s} \approx 3$ tank cycles). For case V1

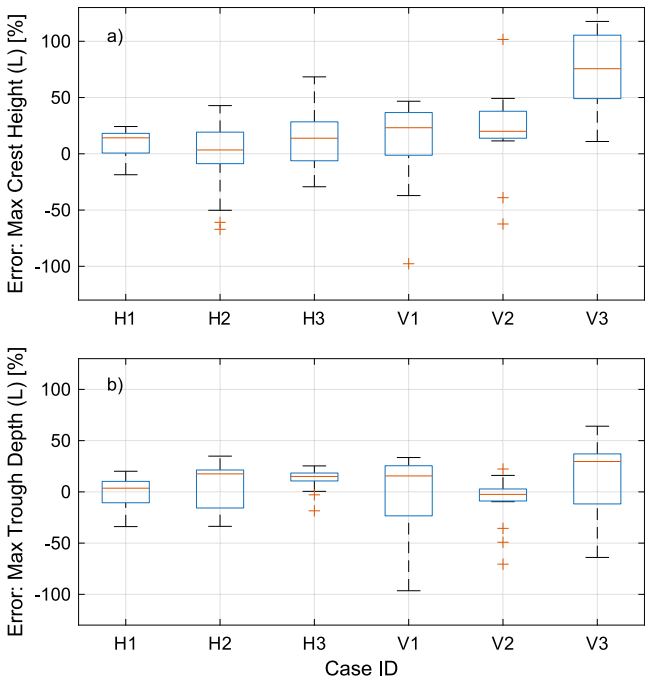

Fig. 12. Box plots showing the distribution of errors in maximum crest height (a) and minimum trough depth (b) for each test case across the numerical solutions. The data presented is for the left sidewall.

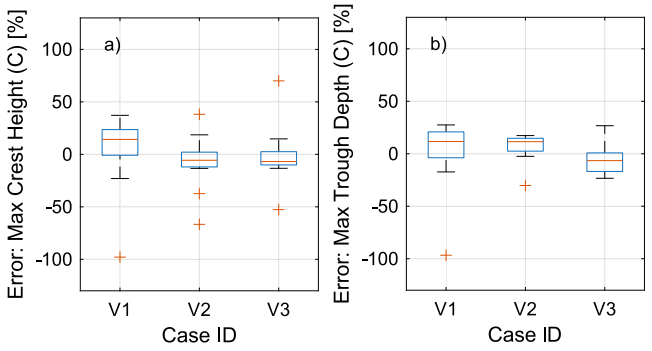

Fig. 13. Box plots showing the distribution of errors in maximum crest height (a) and minimum trough depth (b) for each vertical excitation test case across the numerical solutions. The data presented is for the centre of the tank.

however, capturing the onset time has been shown to be a challenge for the numerical models, with significant discrepancies with the physical modelling (median ≈ -38 s), and large variability between the setups. The cause of this sensitivity is unclear, but could be linked with under-prediction of damping, which is consistent with the over-prediction of displacements in the vertical excitation cases. Given the smaller excitation in case V1, any under-prediction in damping will likely have a more significant impact. It is noted that one numerical model performed better than the others in this metric (-5 s); this is the SPH2 solution which performed well in all cases considered (H1, V1, and V2).

6.4. Maximum crest height and trough depth

When the analysis is further reduced to the maximum crest height and maximum trough depth, the spread in error increases noticeably compared with the full time series evaluation (Fig. 12 and Fig. 13). Considering only the maximum crest height at the left wall (Fig. 12a), median errors rise to around 20%, with a clear tendency for numerical models to over-estimate the crest. The largest variability occurs in the strongly nonlinear cases, particularly V3 and H2.

For the maximum trough depth at the left wall (Fig. 12b), the errors are slightly smaller and more symmetrically distributed about zero, indicating a mix of over- and under-prediction across models. At the centre location, both crest (Fig. 13a) and trough (Fig. 13b) estimates cluster more closely around zero than at the sidewalls, again showing no consistent bias towards under- or over-prediction. Overall, crest over-estimation is most prominent at the sidewalls, while behaviour elsewhere tends to show a more balanced distribution of errors.

7. Conclusions

The numerical results submitted to 'CCP-WSI Blind Test Series 5: isothermal sloshing in a circular tank' are presented and compared with the corresponding physical data. The assessment metrics focus on free surface displacement at the sidewalls and at the centre of the tank, with horizontal and vertical excitation considered independently. The most common approaches among participants were FVM or FDM combined with a VOF scheme, and SPH. Most models successfully capture the dominant frequency in each case, as well as the beat frequency where applicable; however, the accuracy with which the damping of the beating is reproduced varies significantly between setups.

For the horizontal excitation cases, the typical error at the left sidewall is approximately 10–15%, although some participants achieved improved accuracy in the range of 2–5%. This improvement is not fully consistent across all cases; nevertheless, solutions FVM5 (an FVM–VOF approach) and SPH2 (an SPH approach) generally perform well. Further investigation of these setups is recommended to identify the factors contributing to their improved performance. One notable outlier in the results is the case H2 at the right sidewall, which exhibited a pronounced asymmetry in the physical experiment that is not captured by the numerical models.

For vertical excitation, accurately capturing the onset of excitation remains challenging for all numerical models, particularly for case V1, which represents the least severe forcing. Errors at the centre of the tank are generally in the range of 5–15%, while errors at the sidewalls are typically larger, especially in case V3, where significant wave breaking occurs (20–25%). In general, damping appears to be under-predicted across all numerical models, resulting in over-estimated run-up and free surface elevations. It could be that this under-prediction primarily arises from limitations in the models' ability to maintain accurate volume (or mass) conservation during violent free surface deformations, as opposed to an inherent deficiency in capturing viscous or turbulent energy dissipation mechanisms. This requires consideration in future work, focusing on the energy variation and dissipation rates as opposed to the free surface point measurements presented here. In the most extreme case (V3), the median error in maximum elevation reaches +75%. This behaviour is likely exacerbated by difficulties in tracking the free surface during separation and aeration events, as well as inconsistencies in defining the bulk fluid region.

Despite these over-predictions, the qualitative behaviour of the numerical solutions is generally reasonable. Although full free surface profiles were not requested as part of the blind test, they were provided by FVM5. Qualitative comparison with the experimental image data shows strong similarities in the free surface evolution, suggesting that the underlying sloshing dynamics are captured. However, further work is required to accurately reproduce the observed damping. Future studies will therefore focus on identifying the model parameters to which the results are most sensitive, using a systematic approach that isolates individual variables. Additionally, some participants reported issues related to numerical instability; the inherent limitations of each modelling approach should also be considered in future work.

CRediT authorship contribution statement

S.A. Brown: Writing – original draft, Visualization, Project administration, Methodology, Investigation, Formal analysis, Conceptualization. **S.W. Colville:** Writing – original draft, Visualization, Project administration, Methodology, Investigation, Formal analysis, Conceptualization. **V. Francis:** Writing – review & editing, Writing – original draft, Methodology, Investigation. **T. Zhao:** Writing – review & editing, Project administration, Methodology, Investigation. **Y.C. Lee:** Writing – review & editing, Supervision, Funding acquisition, Conceptualization. **D. Cao:** Writing – review & editing, Methodology, Investigation. **H. Chen:** Writing – review & editing, Methodology, Investigation. **J. Chen:** Writing – review & editing, Methodology, Investigation. **S. Chen:** Writing – review & editing, Methodology, Investigation. **J. Davidson:** Writing – review & editing, Methodology, Investigation. **J. Gong:** Writing – review & editing, Methodology, Investigation. **H. Gu:** Writing – review & editing, Methodology, Investigation. **A. Khayyer:** Writing – review & editing, Methodology, Investigation. **D.-H. Kim:** Writing – review & editing, Methodology, Investigation. **W. Liu:** Writing – review & editing, Methodology, Investigation. **M. Luo:** Writing – review & editing, Methodology, Investigation. **R. Lyu:** Writing – review & editing, Methodology, Investigation. **Q. Ma:** Writing – review & editing, Methodology, Investigation. **H. Ma:** Writing – review & editing, Methodology, Investigation. **O. Mahfoze:** Writing – review & editing, Methodology, Investigation. **I. Pregnan Johannesen:** Writing – review & editing, Methodology, Investigation. **Y. Qin:** Writing – review & editing, Methodology, Investigation. **S. Shrestha:** Writing – review & editing, Methodology, Investigation. **G. Tabor:** Writing – review & editing, Methodology, Investigation. **R. Tan:** Writing – review & editing, Methodology, Investigation. **E. Wahbah Makhoul:** Writing – review & editing, Methodology, Investigation. **D. Wang:** Writing – review & editing, Methodology, Investigation. **Y. Wang:** Writing – review & editing, Methodology, Investigation. **H. Wei:** Writing – review & editing, Methodology, Investigation. **S. Yan:** Writing – review & editing, Methodology, Investigation. **K.-K. Yang:** Writing – review & editing, Methodology, Investigation. **Y. Yang:** Writing – review & editing, Methodology, Investigation. **H. Zeng:** Writing – review & editing, Methodology, Investigation. **Y. Zhan:** Writing – review & editing, Methodology, Investigation. **N. Zhang:** Writing – review & editing, Methodology, Investigation. **D.M. Greaves:** Writing – review & editing, Supervision, Funding acquisition, Conceptualization.

Declaration of competing interest

The authors declare the following financial interests/personal relationships which may be considered as potential competing interests: Given their role as an editorial board member, Deborah Greaves and Abbas Khayyer had no involvement in the peer review of this article and had no access to information regarding its peer review. Full responsibility for the editorial process for this article was delegated to another journal editor. Given their role as a guest editor for the special issue "Sloshing of Liquid Hydrogen Fuel Tanks", Scott Brown, Tianyang Zhao and Deborah Greaves had no involvement in the peer review of this article and had no access to information regarding its peer review. Full responsibility for the editorial process for this article was delegated to another journal editor. If there are other authors, they declare that they have no known competing financial interests or personal relationships that could have appeared to influence the work reported in this paper.

Acknowledgements

The CCP-WSI Working Group would like to acknowledge the participants of the CCP-WSI Blind Test Series 5 for their contributions as well as the International Ocean and Polar Engineering (ISOPE) Conference organisers for their support. This work is funded by the Engineering and Physical Sciences Research Council (EPSRC) through projects CCP-WSI+ (EP/T026782/1), HEC-WSI (EP/X035751/1) with additional support from The Computational Science Centre for Research Communities (CoSeC). W. Liu and O. Mahfoze were partially funded by the HASTA project (Grant No. 101138003) as part of the European Union Horizon research program.

Data availability

The full physical dataset from the CCP-WSI Blind Test Series 5 is available as a long standing test case for future benchmarking (CCP-WSI Working Group, 2025; Brown et al., 2025). Please note that the original IDs for each case are 2HIBT5 (H1), 3HIBT5 (H2), 4HIBT5 (H3), 1VIBT5 (V1), 2VIBT5 (V2), and 3VIBT5 (V3).

References

Benjamin, T.B., Ursell, F.J., 1954. The stability of the plane free surface of a liquid in vertical periodic motion. Proc. R. Soc. Lond. Ser. A. Math. Phys. Sci. 225, 505–515. http://dx.doi.org/10.1098/rspa.1954.0218.

Brackbill, J., Kothe, D., Zemach, C., 1992. A continuum method for modeling surface tension. J. Comput. Phys. 100 (2), 335–354. http://dx.doi.org/10.1016/0021-9991(92)90240-Y.

Brown, S., Colville, S., Lee, Y., Greaves, D., 2025. Isothermal sloshing in a circular tank (CCP-WSI Test Case 017 Dataset). http://dx.doi.org/10.24382/1648f8b5-5582-44e5-8e6f-8f95c360b339, University of Plymouth.

Brown, S., Francis, V., Colville, S., Pregnan Johanessen, I., Zhao, T., Greaves, D., 2026. CCP-WSI Blind Test Series 5: Numerical investigation of isothermal sloshing in a circular tank using OpenFOAM. Int. J. Offshore Polar Eng. accepted.

CCP-WSI Working Group, 2025. CCP-WSI Test Case 017 (Blind Test Series 5): Isothermal sloshing in a circular tank. https://ccp-wsi.ac.uk/catalogue/test_cases/test_case_017. (Accessed: 12 May 2026).

Chen, B.-F., Nokes, R., 2005. Time-independent finite difference analysis of fully nonlinear and viscous fluid sloshing in a rectangular tank. J. Comput. Phys. 209 (1), 47–81. http://dx.doi.org/10.1016/j.jcp.2005.03.006.

Chen, J., Yang, Y., Hann, M., Rawlinson-Smith, R., Raji, M., Greaves, D., 2025. SPH simulation of isothermal sloshing in a circular tank: A CCP-WSI blind test study. In: ISOPE International Ocean and Polar Engineering Conference. ISOPE, pp. ISOPE–I–25–333.

Colagrossi, A., Colicchio, G., Lugni, C., Brocchini, M., 2010. A study of violent sloshing wave impacts using an improved SPH method. J. Hydraul. Res. 48 (sup1), 94–104. http://dx.doi.org/10.1080/00221686.2010.9641250.

Colville, S.W., Scolan, Y.-M., Gambioli, F., Greaves, D., Ransley, E., Lee, Y.C., 2025. Faraday waves and period tripling in a horizontal circular tank. J. Fluid Mech. 1006, A4. http://dx.doi.org/10.1017/jfm.2025.16.

Dias, F., Ghidaglia, J.-M., Le Coq, G., 2007. On the fluid dynamics models for sloshing. In: ISOPE International Ocean and Polar Engineering Conference. pp. ISOPE–I–07–565.

Domínguez, J., Fourtakas, G., Altomare, C., Canelas, R., Tafuni, A., García-Feal, O., Martínez-Estévez, I., Mokos, A., Vacondio, R., Crespo, A., Rogers, B., Stansby, P., Gómez-Gesteira, M., 2022. DualSPHysics: from fluid dynamics to multiphysics problems. Comput. Part. Mech. 9 (5), 867–895. http://dx.doi.org/10.1007/s40571-021-00404-2.

ESI OpenCFD, 2018. OpenFOAM-v1812. https://www.openfoam.com/news/main-news/openfoam-v1812. (Accessed: 12 May 2026).

ESI OpenCFD, 2020. OpenFOAM-v2006. https://www.openfoam.com/news/main-news/openfoam-v2006. (Accessed: 12 May 2026).

ESI OpenCFD, 2022. OpenFOAM-v2212. https://www.openfoam.com/news/main-news/openfoam-v2212. (Accessed: 12 May 2026).

ESI OpenCFD, 2023. OpenFOAM-v2312. https://www.openfoam.com/news/main-news/openfoam-v2312. (Accessed: 12 May 2026).

Faltinsen, O.M., 1978. A numerical nonlinear method of sloshing in tanks with two-dimensional flow. J. Ship Res. 22 (03), 193–202. http://dx.doi.org/10.5957/jsr.1978.22.3.193.

Faltinsen, O.M., Rognebakke, O.F., Lukovsky, I.A., Timokha, A.N., 2000. Multidimensional modal analysis of nonlinear sloshing in a rectangular tank with finite water depth. J. Fluid Mech. 407, 201–234. http://dx.doi.org/10.1017/S0022112099007569.

Faltinsen, O.M., Timokha, A.N., 2001. An adaptive multimodal approach to nonlinear sloshing in a rectangular tank. J. Fluid Mech. 432, 167–200. http://dx.doi.org/10.1017/S0022112000003311.

Faltinsen, O.M., Timokha, A.N., 2009. Sloshing, vol. 577, Cambridge university press Cambridge.

Gu, H., Ren, A., Wang, D., Zang, J., Thiruvenkatasamy, K., Moreno, E., 2025. Simulation of liquid sloshing using virtual boundary force method in non-inertial coordinates. In: Proceedings of the 35th International Ocean and Polar Engineering Conference. pp. ISOPE–I–25–336.

Hirt, C.W., Nichols, B.D., 1981. Volume of fluid (VOF) method for the dynamics of free boundaries. J. Comput. Phys. 39 (1), 201–225. http://dx.doi.org/10.1016/0021-9991(81)90145-5.

Huang, P., 2023. A comprehensive investigation on liquid sloshing of rectangular water tank with vertical baffles. Ocean Eng. 288, 116126. http://dx.doi.org/10.1016/j.oceaneng.2023.116126.

Ibrahim, R.A., 2005. Liquid sloshing dynamics: theory and applications. Cambridge University Press, http://dx.doi.org/10.1017/CBO9780511536656.

Ibrahim, R.A., 2020. Assessment of breaking waves and liquid sloshing impact. Nonlinear Dynam. 100 (3), 1837–1925. http://dx.doi.org/10.1007/s11071-020-05605-7.

Jäger, M., 2019. Fuel Tank Sloshing Simulation Using the Finite Volume Method. Springer.

Kim, K.S., Kim, M.H., Park, J.-C., 2014. Development of moving particle simulation method for multiliquid-layer sloshing. Math. Probl. Eng. 2014 (1), 350165. http://dx.doi.org/10.1155/2014/350165.

Kim, D.-H., Yang, K.-K., 2025. Numerical study of free-surface behavior in sloshing flows within a circular tank. In: Proceedings of the 35th International Ocean and Polar Engineering Conference. pp. ISOPE–I–25–602.

Konar, T., Das, A., 2025. A review of numerical modelling of liquid sloshing in partially filled containers. Ships Offshore Struct. 1–26. http://dx.doi.org/10.1080/17445302.2025.2491080.

Lin, P., Cheng, L., Liu, D., 2016. A two-phase flow model for wave–structure interaction using a virtual boundary force method. Comput. & Fluids 129, 101–110. http://dx.doi.org/10.1016/j.compfluid.2016.02.007.

Liu, D., Lin, P., 2008. A numerical study of three-dimensional liquid sloshing in tanks. J. Comput. Phys. 227 (8), 3921–3939. http://dx.doi.org/10.1016/j.jcp.2007.12.006.

Ma, H., Chen, S., Wei, H., Wang, Y., Lyu, R., 2025. Numerical study of multi-phase isothermal sloshing in a circular tank using DualSPHysics. In: Proceedings of the 35th International Ocean and Polar Engineering Conference. pp. ISOPE–I–25–340.

McIver, P., 1989. Sloshing frequencies for cylindrical and spherical containers filled to an arbitrary depth. J. Fluid Mech. 201, 243–257. http://dx.doi.org/10.1017/S0022112089000923.

Oxtoby, O.F., Malan, A., Heyns, J.A., 2015. A computationally efficient 3D finite-volume scheme for violent liquid–gas sloshing. Internat. J. Numer. Methods Fluids 79 (6), 306–321. http://dx.doi.org/10.1002/fld.4055.

Pan, X.-j., Zhang, H.-x., Lu, Y.-t., 2008. Numerical simulation of viscous liquid sloshing by moving-particle semi-implicit method. J. Mar. Sci. Appl. 7 (3), 184–189. http://dx.doi.org/10.1007/s11804-008-7047-3.

Peric, M., Zorn, T., el Moctar, O., Schellin, T.E., Kim, Y.-S., 2009. Simulation of sloshing in LNG-tanks. J. Offshore Mech. Arct. Eng. 131, http://dx.doi.org/10.1115/1.3058688.

Qin, Y., Gong, J., 2025. Investigation of isothermal sloshing dynamics in circular tank. In: Proceedings of the 35th International Ocean and Polar Engineering Conference. pp. ISOPE–I–25–335.

Rafiee, A., Pistani, F., Thiagarajan, K., 2011. Study of liquid sloshing: numerical and experimental approach. Comput. Mech. 47 (1), 65–75. http://dx.doi.org/10.1007/s00466-010-0529-6.

Ransley, E., Brown, S., Hann, M., Greaves, D., Windt, C., Ringwood, J., et al., 2020a. A blind comparative study of focused wave interactions with floating structures (CCP-WSI Blind Test Series 2). Proc. Inst. Civ. Eng. - Eng. Comput. Mech. 174 (1), 46–61. http://dx.doi.org/10.1680/jencm.20.00006.

Ransley, E., Yan, S., Brown, S., Hann, M., Graham, D., Windt, C., et al., 2020b. A blind comparative study of focused wave interactions with floating structures (CCP-WSI Blind Test Series 3). Int. J. Offshore Polar Eng. 30 (01), 1–10. http://dx.doi.org/10.17736/ijope.2020.jc774.

Ransley, E., Yan, S., Brown, S.A., Mai, T., Graham, D., Ma, Q., et al., 2019. A blind comparative study of focused wave interactions with a fixed FPSO-like structure (CCP-WSI Blind Test Series 1). Int. J. Offshore Polar Eng. 29 (02), 113–127. http://dx.doi.org/10.17736/ijope.2019.jc748.

Rudman, M., Cleary, P.W., Prakash, M., 2009. Simulation of liquid sloshing in model LNG tank using smoothed particle hydrodynamics. Int. J. Offshore Polar Eng. 19 (04).

Sanapala, V., Selvaraj, T., Ananthasivan, K., Patnaik, B., 2024. Numerical simulation of wave impact and high pressure characteristics due to violent sloshing in a rectangular tank. Ships Offshore Struct. 19 (5), 625–643. http://dx.doi.org/10.1080/17445302.2023.2195258.

Schreier, S., Paschen, M., 2008. Sloshing in LNG tanks: assessment of high and low pressures. In: International Conference on Offshore Mechanics and Arctic Engineering, vol. 48227, pp. 935–941. http://dx.doi.org/10.1115/OMAE2008-57858.

Shao, J., Li, H., Liu, G., Liu, M., 2012. An improved SPH method for modeling liquid sloshing dynamics. Comput. Struct. 100, 18–26. http://dx.doi.org/10.1016/j.compstruc.2012.02.005.

Siemens Digital Industries Software, 2026. STAR-CCM+. https://plm.sw.siemens.com/en-US/simcenter/fluids-thermal-simulation/star-ccm/. (Accessed: 12 May 2026).

Sussman, M., Smereka, P., Osher, S., 1994. A level set approach for computing solutions to incompressible two-phase flow. J. Comput. Phys. 114 (1), 146–159. http://dx.doi.org/10.1006/jcph.1994.1155.

Tan, R., Mahfoze, O., Liu, W., 2025. Hydrodynamic study of sloshing in a horizontally and vertically excited cylinder. In: Proceedings of the 35th International Ocean and Polar Engineering Conference. pp. ISOPE–I–25–331.

The OpenFOAM Foundation, 2015. OpenFOAM-v3.0.0. https://openfoam.org/release/3-0-0/. (Accessed: 12 May 2026).

Thiagarajan, K., Rakshit, D., Repalle, N., 2011. The air–water sloshing problem: Fundamental analysis and parametric studies on excitation and fill levels. Ocean Eng. 38 (2–3), 498–508. http://dx.doi.org/10.1016/j.oceaneng.2010.11.019.

Tuyen, L., Ang, K., HAI, L., 2013. Sloshing effect and mitigation solution of floating oil storage tank. In: Proceedings of the Thirteenth East Asia-Pacific Conference on Structural Engineering and Construction (EASEC-13). pp. I–2–2.

Wang, D., Dong, S., 2024. Two-dimensional numerical modelling of a novel heaving wave energy converter-perforated breakwater integrated system. Appl. Ocean Res. 153, 104274. http://dx.doi.org/10.1016/j.apor.2024.104274.

Wang, D., Gu, H., Ren, B., 2025. Numerical simulation of the CCP-WSI Blind Test Series 5: isothermal sloshing in a circular tank. In: Proceedings of the 35th International Ocean and Polar Engineering Conference. pp. ISOPE–I–25–341.

Weller, H.G., Tabor, G., Jasak, H., Fureby, C., 1998. A tensorial approach to computational continuum mechanics using object-oriented techniques. Comput. Phys. 12 (6), 620–631. http://dx.doi.org/10.1063/1.168744.

Wu, C.-H., Chen, B.-F., 2009. Sloshing waves and resonance modes of fluid in a 3D tank by a time-independent finite difference method. Ocean Eng. 36 (6–7), 500–510. http://dx.doi.org/10.1016/j.oceaneng.2009.01.020.

Wu, C.-H., Chen, B.-F., Hung, T.-K., 2013. Hydrodynamic forces induced by transient sloshing in a 3D rectangular tank due to oblique horizontal excitation. Comput. Math. Appl. 65 (8), 1163–1186. http://dx.doi.org/10.1016/j.camwa.2013.02.012.

Young Yoon, H., Koshizuka, S., Oka, Y., 1999. A particle–gridless hybrid method for incompressible flows. Internat. J. Numer. Methods Fluids 30 (4), 407–424. http://dx.doi.org/10.1002/(SICI)1097-0363(19990630)30:4<407::AID-FLD846>3.0.CO;2-C.

Yu, S., Ransley, E., Qian, L., Zhou, Y., Brown, S., Greaves, D., et al., 2025. Modelling the hydrodynamic response of a floating offshore wind turbine – a comparative study. Appl. Ocean Res. 155, 104441. http://dx.doi.org/10.1016/j.apor.2025.104441.

Zeng, H., Chen, H., Lu, T., Lin, Z., He, J., Cao, D., 2025. Numerical study of the fluid sloshing in a horizontal cylinder due to horizontal and vertical excitation. In: Proceedings of the 35th International Ocean and Polar Engineering Conference. pp. ISOPE–I–25–342.

Zhan, Y., Luo, M., Khayyer, A., 2025. DualSPHysics+: An enhanced DualSPHysics with improvements in accuracy, energy conservation and resolution of the continuity equation. Comput. Phys. Comm. (ISSN: 0010-4655) 306, 109389. http://dx.doi.org/10.1016/j.cpc.2024.109389.

Zhang, N., Ni, B., Xue, Y., Zan, Y., Zeng, Q., Yan, S., Ma, Q., 2025. Numerical study of sloshing in a circular tank by a GNN supported isph method. In: Proceedings of the 35th International Ocean and Polar Engineering Conference. pp. ISOPE–I–25–334.

Zhang, N., Yan, S., Ma, Q., Li, Q., 2024. A hybrid method combining ISPH with graph neural network for simulating free-surface flows. Comput. Phys. Comm. 301, 109220. http://dx.doi.org/10.1016/j.cpc.2024.109220.